Check for updates

AGU ADVANCING EARTH AND SPACE SCIENCE

Earth and Space Science

TECHNICAL REPORTS: METHODS

10.1029/2020EA001097

Special Section:
Nonlinear Systems in Geophysics: Past Accomplishments and Future Challenges

Nowcasting Earthquakes in Southern California With Machine Learning: Bursts, Swarms, and Aftershocks May Be Related to Levels of Regional Tectonic Stress

John B. Rundle[1,2,3] and Andrea Donnellan[4]

[1]Department of Physics, University of California, Davis, CA, USA, [2]Santa Fe Institute, Santa Fe, NM, USA, [3]Department of Earth and Planetary Science, University of California, Davis, CA, USA, [4]Jet Propulsion Laboratory, California Institute of Technology, Pasadena, CA, USA

Key Points:
- A new nowcasting method using earthquake swarms and aftershocks reveals the hazard from large $M \geq 7$ earthquakes in Southern California
- Machine learning defines a time series of bursts using an exponential moving average filtered and optimized to reveal temporal structure
- Cycles of recharge and discharge associated with $M \geq 7$ earthquakes are revealed, reminiscent of stress accumulation and release

Correspondence to:
J. B. Rundle,
jbrundle@ucdavis.edu

Citation:
Rundle, J. B., & Donnellan, A. (2020). Nowcasting earthquakes in Southern California with machine learning: Bursts, swarms, and aftershocks may be related to levels of regional tectonic stress. *Earth and Space Science*, *7*, e2020EA001097. https://doi.org/10.1029/2020EA001097

Received 16 JAN 2020
Accepted 9 AUG 2020
Accepted article online 25 AUG 2020

Abstract

Seismic bursts in Southern California are sequences of small earthquakes strongly clustered in space and time and include seismic swarms and aftershock sequences. A readily observable property of these events, the radius of gyration (R_G), allows us to connect the bursts to the temporal occurrence of the largest $M \geq 7$ earthquakes in California since 1984. In the Southern California earthquake catalog, we identify hundreds of these potentially coherent space-time structures in a region defined by a circle of radius 600 km around Los Angeles. We compute R_G for each cluster then filter them to identify those bursts with large numbers of events closely clustered in space, which we call "compact" bursts. Our basic assumption is that these compact bursts reflect the dynamics associated with large earthquakes. Once we have filtered the burst catalog, we apply an exponential moving average to construct a time series for the Southern California region. We observe that the R_G of these bursts systematically decreases prior to large earthquakes, in a process that we might term "radial localization." The R_G then rapidly increases during an aftershock sequence, and a new cycle of "radial localization" then begins. These time series display cycles of recharge and discharge reminiscent of seismic stress accumulation and release in the elastic rebound process. The complex burst dynamics we observe are evidently a property of the region as a whole, rather than being associated with individual faults. This new method allows us to improve earthquake nowcasting, which is a technique to evaluate the current state of hazard in a seismically active region.

Plain Language Summary

Earthquake nowcasting is a method to evaluate the current state of seismic hazard from large earthquakes. In this paper, we connect the temporal occurrence of the largest and most potentially destructive earthquakes in California since 1984 with a readily observable property of small earthquake seismicity in the region. Our method involves the calculation of the time history of the average radius (horizontal size or extent) of "bursts" of small earthquakes, in the time leading up to and following major earthquakes in the region. We observe that the radius systematically and gradually decreases leading up to major earthquakes, increasing suddenly and discontinuously following the event. This *observable* pattern resembles the long-hypothesized cycle of regional tectonic stress buildup and release, or elastic rebound, associated with large destructive earthquakes. We propose that the radius of these bursts might be considered to be a proxy variable for the changing state of regional stress in Southern California.

1. Introduction

Earthquakes of all magnitudes are known to cluster strongly in space and time (e.g., Reasenberg, 1985; Scholz, 2019). In fact, such burst phenomena are widely observed in many areas of science (Bahar et al., 2015; Mantegna & Stanley, 2004; Paczuski et al., 1996). For purposes of convenience, we introduce here a definition of seismic bursts that encompasses both seismic swarms and aftershock sequences, but that could be applied to other types of clustered events.

The goal of our work is to improve upon the methods of earthquake nowcasting (Rundle, Giguere, et al., 2019; Rundle, Luginbuhl, et al., 2019; Rundle et al., 2002, 2016, 2018), which can be used to define the current state of risk from large earthquakes. These methods have begun to be applied to India (Pasari, 2019), Japan (K. Nanjo, personal communication, January, 2020), and Greece (G. Chouliaris personal communication, July, 2019).

©2020. The Authors.
This is an open access article under the terms of the Creative Commons Attribution-NonCommercial-NoDerivs License, which permits use and distribution in any medium, provided the original work is properly cited, the use is non-commercial and no modifications or adaptations are made.

10.1029/2020EA001097

Our definition of a seismic burst is the occurrence of an unusual sequence of earthquakes closely clustered in space and time (e.g., Hill & Prejean, 2007; Peresan & Gentili, 2018; Zaliapin & Ben-Zion, 2016a, 2016b).

We define two general types of bursts, Type I and Type II:

- We define a Type I seismic burst as a mainshock-aftershock sequence, in which the initiating event has the largest magnitude in the sequence and is typically followed by a power law Omori decay of occurrence of smaller events (Omori, 1894; Scholz, 2019).
- A Type II seismic burst is defined as a sequence of similar magnitude events in which the largest-magnitude event is not the initiating event and in which there is not typically a subsequent power law decay.

The earthquakes defining the bursts are small, usually of magnitudes characterizing the catalog completeness level. For the Southern California region, we consider small earthquakes of magnitudes $M \geq 3.3$. This magnitude threshold was chosen as a value high enough to ensure completeness of the catalog data used. The catalog containing these events is downloaded from the U.S. Geological Survey earthquake search database (https://earthquake.usgs.gov/earthquakes/search/).

In our analysis below, we consider the Southern California region contained within a 600-km circle surrounding Los Angeles, California. We also consider time series beginning after 1 January 1984, after the data became most reliable in terms of catalog completeness, with accurate locations. The region is arbitrary in terms of method but requires a complete catalog to be adequately applied and tested. If small earthquakes are missing from the catalog, the clusters so defined will likewise not be correctly defined, they will have missing events. Or potentially important clusters will not be present at all.

2. Method

We begin with our definition of a seismic burst or cluster of small events. We coarse-grain time in the catalog into units of single days and consider an elementary burst to be a day on which there are two or more small earthquakes of magnitude $M \geq 3.3$ within the region of interest, which for this study is the 600-km radius Southern California region. Note that, over the last 10 years, the rate of occurrence of these small earthquakes has been about 0.75 such earthquakes per day in that geographic region.

The method we describe proceeds in five stages. The first stage consists of an automated definition and classification of seismicity into candidates of seismic bursts. The second stage involves automated rejection of outliers. The third stage selects the members of the ensemble of accepted bursts, which will then be displayed as a time series. The fourth stage applies an exponential moving average (EMA) to the bursts to construct the burst time series. The fifth stage involves optimization of the ensemble of possible bursts with a simple cost function. We note that both classification/clustering and optimization/regression are well-known components of new ideas in machine learning, along with other ideas in deep learning and decision tree analysis (https://en.wikipedia.org/wiki/Machine_learning).

2.1. Unsupervised Learning (Clustering)

In Stage I, classification, the daily seismic catalog is searched to find bursts consisting of connected sequences of days in which two or more $M \geq 3.3$ events occur without any intervening days of fewer events. For each such set of days, we also, as a rule, include the preceding day to allow for any foreshock events.

This stage yields many hundreds of candidate bursts. Note that this process will of necessity yield bursts that include purely random, uncorrelated events. To remove these, we then filter the bursts in the following two ways.

In Stage II of the method, rejection of outliers, we detect and remove small earthquakes that may be random outliers. We begin by computing the spatial centroid, or center of mass, of each burst. In this calculation, all events having $M \geq 3.3$ are treated as a particle or unit of mass, each of equal computational weight.

We now compute the horizontal distance or radius ("R_i") of each small event from the centroid, then the median distance ("MedianR") is calculated from the set $\{R_i\}$. A factor F_{CL} is defined such that if any event in the burst satisfies the relation:

23335084, 2020, 9, Downloaded from https://agupubs.onlinelibrary.wiley.com/doi/10.1029/2020EA001097 by Birla Institute of Technology & Science - Pilani, Wiley Online Library on [27/06/2024]. See the Terms and Conditions (https://onlinelibrary.wiley.com/terms-and-conditions) on Wiley Online Library for rules of use; OA articles are governed by the applicable Creative Commons License

$$R_i > \text{MedianR}^* F_{CL} \qquad \text{(reject)} \tag{1}$$

it is rejected.

This filter is applied to each of the candidate bursts. Using all the accepted small events in the burst, we then compute the burst radius of gyration R_G about the burst centroid. Note that R_G is the square root of the mean square radius of the small events in the burst. These filtered bursts now define the ensemble of accepted clusters. Radius of gyration is a parameter used to study fracture mechanics (e.g., Kucherov & Ryvkin, 2014; Sayers & Calvez, 2010).

As a numerical example, we find that many of the compact clusters of most interest have MedianR ~ 1 km. A typical value of F_{CL} is 5–25 (see below), so that small events farther away than 5 to 25 km from the burst centroid would be rejected.

In Stage III of the method, we filter the collection of bursts according to their mass ratio or density ρ, which we define as the ratio of cluster mass μ to radius of gyration R_G:

$$\rho = \mu / R_G \tag{2}$$

Again, mass is defined as the number of small events in the cluster or burst.

To implement this filter, we define a filter or threshold value F_{EN} corresponding to a particular value of mass ratio ρ. Each burst is tested, with the criterion for *acceptance* being

$$\rho \geq F_{EN} \qquad \text{(accept)}. \tag{3}$$

With this condition, we accept only high-density clusters, which are typically the most compact clusters. As will be seen, clusters that are accepted by this criterion correspond to long wavelength fluctuations in the time series, so Condition 3 represents a low-pass filter.

Since the range of values of F_{EN} is rather large (see below), we prefer to work with $\text{Log}_{10}(\rho)$ or $\text{Log}_{10}(F_{EN})$. The more compact bursts are found to have ρ as large as 10–100 per km, some of these being aftershocks of the major earthquakes that have occurred in the region since 1984.

In Stage IV, we apply an EMA (https://en.wikipedia.org/wiki/Machine_learning) to the filtered burst time series data. The choice to be made with this method is the value of N, the number of averaging steps. For our purposes, we chose to adopt a 1-year averaging interval for the temporal resolution, corresponding to an average of N ~ 23 bursts per year. From this value, we compute the α parameter in the EMA as in the usual formula for the EMA (https://en.wikipedia.org/wiki/Moving_average):

$$a = 2/(N+1). \tag{4}$$

Stage V is described below.

3. Results

3.1. Basic Results

Figure 1 shows an example of a moderate-sized burst with a mass of 23 small events and a radius of gyration of 2.61 km. It began on 31 August 2005 and ended on 2 September 2005. The density, mass-to-radius ratio, of this burst is thus 8.81 km^{-1}. Location was at the southern end of the Salton Sea, with a maximum magnitude of M5.1.

Figure 2 displays a map of filtered burst centroids in the region considered, a circle of radius 600 km around Los Angeles, CA (34.0522°N, 118.2437°W). Here, the large dashed blue circular line defines the 600-km radius circle around Los Angeles that we used. The burst centroids are represented by the points on the map, color coded by their date of occurrence since 1984. Cooler colors represent earlier bursts, and hotter colors represent later bursts.

Figure 3 shows the cluster mass ratios ρ as a function of radius of gyration R_G. Densities are plotted as $\text{Log}_{10}(\rho)$ for convenience and clarity. The horizontal dashed line corresponds to a density $\rho = 1.0$. Bursts

23335084, 2020, 9, Downloaded from https://agupubs.onlinelibrary.wiley.com/doi/10.1029/2020EA001097 by Birla Institute of Technology & Science - Pilani, Wiley Online Library on [27/06/2024]. See the Terms and Conditions (https://onlinelibrary.wiley.com/terms-and-conditions) on Wiley Online Library for rules of use; OA articles are governed by the applicable Creative Commons License

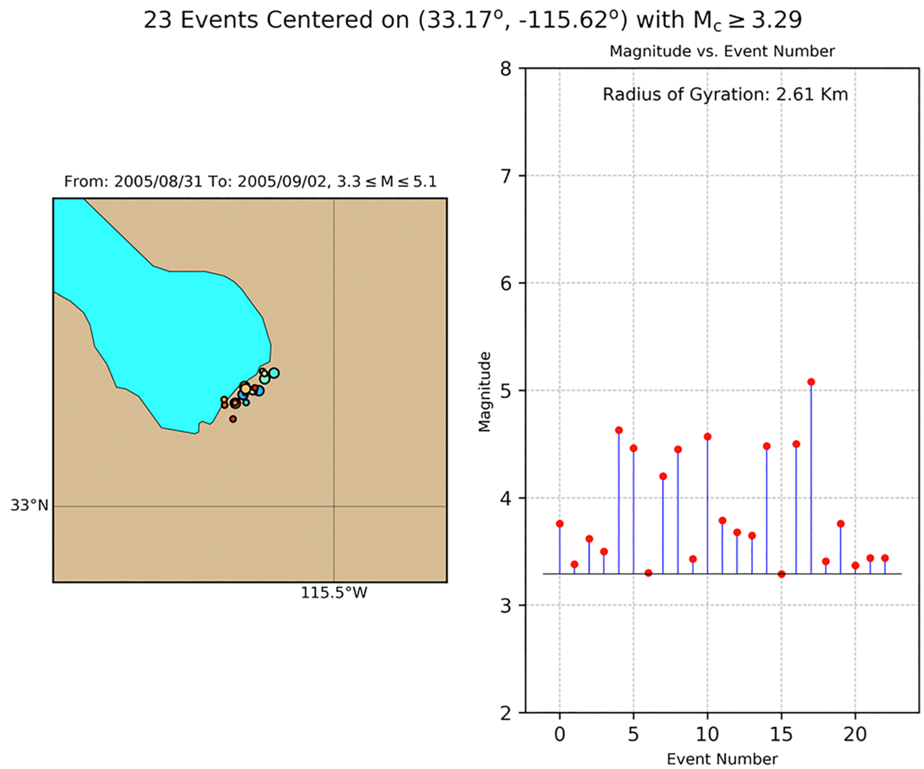

Figure 1. Example of a moderate burst. (left) Map of epicenters. Symbol color:cooler colors represent earlier events in the burst, and hotter colors later events. Symbol size represents magnitudes. (right) Magnitudes of the sequence of events in the burst.

with mass ratios above the dashed horizontal line are accepted by the ensemble filter. These bursts are used to plot the time series in Figure 4.

As an example of the EMA time series we compute, Figure 4 shows burst radius of gyration R_G as a function of time since 1 January 1984, constructed using the filtered bursts and the EMA. Note that the vertical axis is inverted so that an increasing or rising curve represents a progressively smaller value of R_G. Filter values are $F_{CL} = 25$, $F_{EN} = 1.0$. Dots represent the bursts used in constructing the figure, and blue dashed lines are interpolated values between the bursts.

In Figure 4 the four vertical red dashed lines record the dates of the $M \geq 7.0$ earthquakes in the region since 1984: M7.3 Landers, 28 June 1984; M7.1 Hector Mine, 16 October 1999; M7.2 El Major Cucupah, 4 April 2010; and M7.1 Ridgecrest, 5 July 2019. It can be seen that the EMA time series progressively increases prior to the $M \geq 7.0$ events, such that the value of R_G progressively declines, reaching a value less than about $R_G \sim 2$ km, after which the large $M \geq 7.0$ earthquake occurs. We call this process radial localization, to distinguish it from spatial localization that has been previously proposed and that has been difficult to observe for earthquakes.

The sudden and discontinuous declines in the time series, or increase in R_G, just after the time of the large earthquakes represent the appearance of the aftershock bursts. These are obviously large, very compact bursts with large masses. Radii of gyration R_G are typically the size of the mainshock dimensions, meaning they are much larger than the preseismic, compact small bursts. Thus, on a plot such as Figure 3, these will correspond to a sudden decrease in value of the time series on the inverted scale of the figure, or a sudden increase in radius of gyration.

The other vertical dotted lines represent earthquakes having magnitudes $6.0 \leq M \leq 7.0$. See Table 1 for a list of these. It is interesting to observe that the M6.5 San Simeon earthquake that occurred on 22 December 2003 had a more visible signature in Figure 3 than the M6.7 Northridge earthquake of 17 January 1994. But neither of these earthquakes had a significant effect on the evolution of the time series.

23335084, 2020, 9, Downloaded from https://agupubs.onlinelibrary.wiley.com/doi/10.1029/2020EA001097 by Birla Institute of Technology & Science - Pilani, Wiley Online Library on [27/06/2024]. See the Terms and Conditions (https://onlinelibrary.wiley.com/terms-and-conditions) on Wiley Online Library for rules of use; OA articles are governed by the applicable Creative Commons License

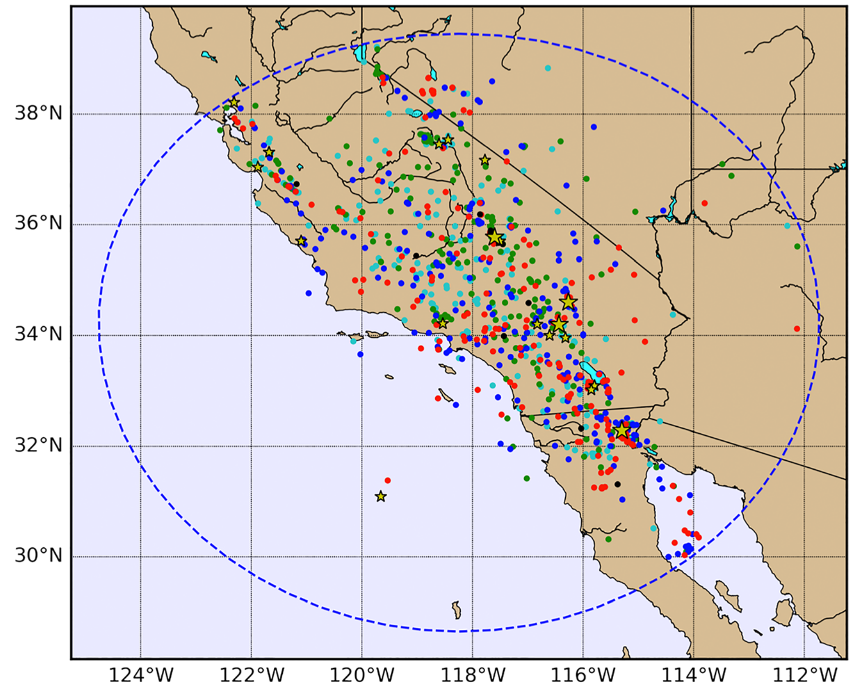

Figure 2. Map of centroids of all 857 bursts from 1 January 1984 to 21 December 2019. Cyan color represent bursts prior to 1992 Landers earthquake (Table 1). Green represents bursts occurring between 1992 landers and 1999 Hector Mine earthquakes, blue color represents bursts between Hector Mine and El Major Cucupah earthquakes, red color between El Major Cucupah and Ridgecrest earthquakes, and black color following Ridgecrest. Larger yellow stars locate the epicenters of the $M \geq 7$ earthquakes during the period, and smaller yellow stars locate the epicenters of the $7.0 > M \geq 6.0$ earthquakes.

Note in particular the sudden increase in R_G (decrease in time series) during 26–28 August 2012, where no vertical dashed line is shown (vertical arrow). This event corresponds to the Brawley earthquake swarm (https://www.usgs.gov/center-news/earthquake-swarm-brawley-seismic-zone) which included two earthquakes having magnitude $M \geq 5$. The occurrence of this sudden increase in R_G may suggest the occurrance of an event more significant than the $M \sim 5$ events, such as a larger slow earthquake.

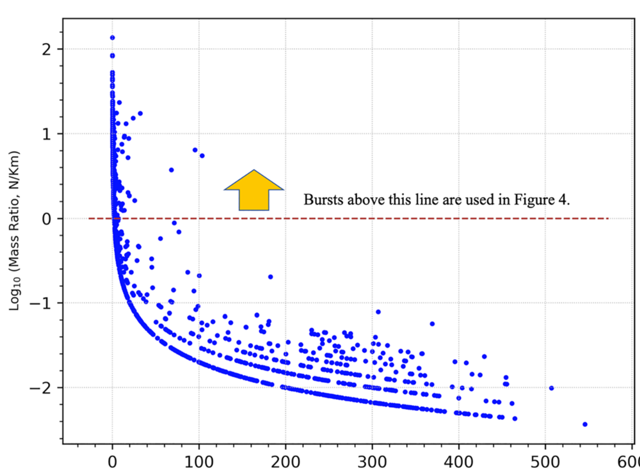

Figure 3. Log_{10} of burst density $\rho =$ (ratio of mass to radius of gyration) as function of radius of gyration. Mass is the number of magnitude $M \geq 3.39$ earthquakes in the burst. Bursts above the dashed horizontal line (arrow) are used to construct the time series in Figure 4 (following).

Other less prominent but similar patterns can be seen, as, for example, in August–September 1995. This event is apparently associated with the Ridgecrest earthquake swarm (https://scedc.caltech.edu/significant/ridgecrest1995.html) that began on 17 August 1995 (vertical arrow). A series of events occurred in that swarm, including a $M5.8$ earthquake that spawned over 2,500 aftershocks in the next weeks.

3.2. Sensitivity

We expect that time series such as that in Figure 4 will be affected by, and sensitive to, the choice of values for F_{CL} and F_{EN}. To illustrate this sensitivity, we show four such time series in Figure 5. These time series are computed for (a) $\text{Log}_{10}(F_{EN}) = -1.0$, $F_{CL} = 25$; (b) $\text{Log}_{10}(F_{EN}) = 0.2$, $F_{CL} = 25$; (c) $\text{Log}_{10}(F_{EN}) = -1.0$, $F_{CL} = 10$; and (d) $\text{Log}_{10}(F_{EN}) = 0.2$, $F_{CL} = 10$.

It can be seen from Figure 5 that the time series have varying amounts of power in the frequency bands that define them. For example, Figures 5a and 5c have more high-frequency information than Figures 5b and 5d. As a result, we adopt a strategy that seeks to bring out the common features of all these time series.

23335084, 2020, 9, Downloaded from https://agupubs.onlinelibrary.wiley.com/doi/10.1029/2020EA001097 by Birla Institute of Technology & Science - Pilani, Wiley Online Library on [27/06/2024]. See the Terms and Conditions (https://onlinelibrary.wiley.com/terms-and-conditions) on Wiley Online Library for rules of use; OA articles are governed by the applicable Creative Commons License

23335084, 2020, 9, Downloaded from https://agupubs.onlinelibrary.wiley.com/doi/10.1029/2020EA001097 by Birla Institute of Technology & Science - Pilani, Wiley Online Library on [27/06/2024]. See the Terms and Conditions (https://onlinelibrary.wiley.com/terms-and-conditions) on Wiley Online Library for rules of use; OA articles are governed by the applicable Creative Commons License

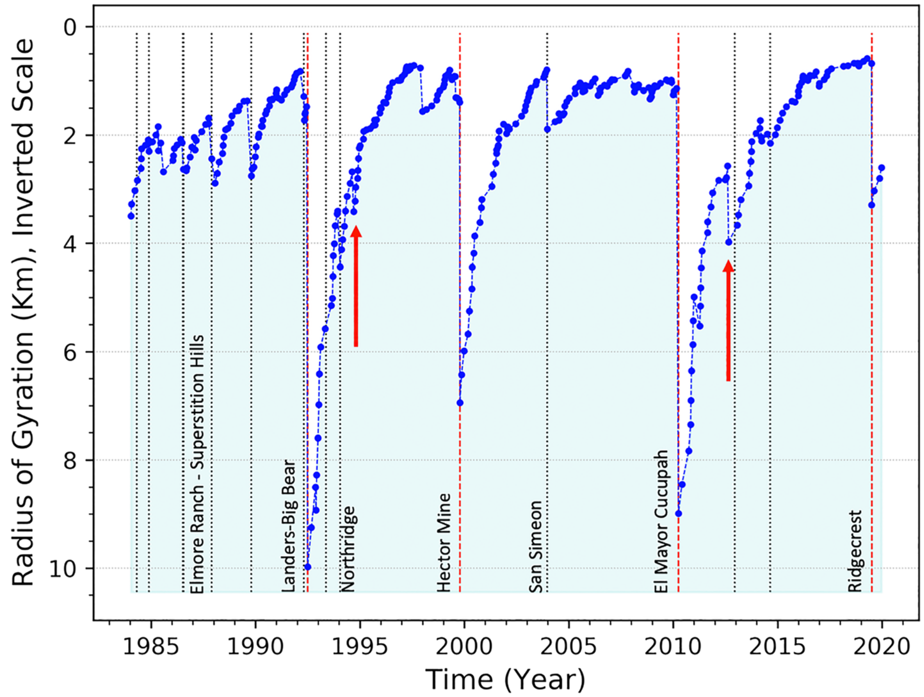

Figure 4. Example of a time series for the exponential moving average (EMA) radius of gyration of bursts in the region using $F_{EN} = 0.0$ and $F_{CL} = 25$ (see text for definitions). A few of the prominent large earthquakes are indicated (Table 1). A value $N = 23$ was used to construct the EMA (see text). Left red arrow indicates the Ridgecrest swarm of 17 August 1995, and right arrow indicates the Brawley swarm of 26 August 2012. Note that the vertical scale is inverted, so that the smallest radius bursts are at the top.

Table 1
Large Earthquakes Near Los Angles From 1 January 1984 to 21 December 2019

Date (Z)	Time (Z)	Magnitude	Location
4-24-1984	21:15:18.760	6.2	Morgan Hill
11-23-1984	18:08:25.360	6.1	Round Valley
7-8-1986	09:20:44.560	6	Morongo Valley
7-21-1986	14:42:26.000	6.4	Chalfant Valley
11-24-1987	01:54:14.660	6.2	Elmore Ranch
11-24-1987	13:15:56.710	6.6	Superstition Hills
10-18-1989	00:04:15.190	6.9	Loma Prieta
4-23-1992	04:50:23.230	6.1	Joshua Tree
6-28-1992	11:57:34.130	7.3	Landers
6-28-1992	15:05:30.730	6.3	Big Bear
5-17-1993	23:20:50.250	6.1	Big Pine
1-17-1994	12:30:55.390	6.7	Northridge
10-16-1999	09:46:44.460	7.1	Ludlow
12-22-2003	19:15:56.240	6.5	San Simeon
4-4-2010	22:40:42.360	7.2	El Major Cucupah
12-14-2012	10:36:01.590	6.3	Baja Coast
8-24-2014	10:20:44.070	6.02	Napa
7-4-2019	17:33:49.000	6.4	Ridgecrest
7-6-2019	03:19:53.040	7.1	Ridgecrest

3.3. Optimization/Regression for Common Features of Earthquakes

In Stage V of our approach, we optimize the collection or ensemble of the bursts and combine them into a single time series using a simple cost function. The result of this stage is an ensemble in which the largest earthquakes of $M \geq 7$ occur at approximately the same value of R_G for each event. We find that an acceptable estimate of the optimal ensemble is equal weighting of the members of the ensemble of values of F_{CL} and F_{EN}, which range from [5,10,...,25], and $\text{Log}_{10}(F_{EN}) = [-1.0, -0.9, ...,0.2]$.

The strategy involves defining a cost function that seeks to optimize the value of radius of gyration R_G for the largest earthquakes $M \geq 7$, just before they occur. The cost function that we use requires that the radius of gyration of these large earthquakes just prior to failure be a relatively uniform value. This would allow a crude forecast of when a large such earthquake might occur in the future.

We construct in Figure 6 an EMA time series by building an ensemble average over many time series similar to that shown in Figure 4. Note that each time series in the ensemble will of necessity be composed of a different number of bursts (blue dots in Figure 4). Also, note that each such time series is tabulated nonuniformly in time.

Constructing such an ensemble average of time series demands that we have an equidistantly tabulated time series for each value of the control variables $[F_{CL}, F_{EN}]$. From each nonuniform time series, we therefore build an interpolated time series having equidistantly tabulated values

10.1029/2020EA001097

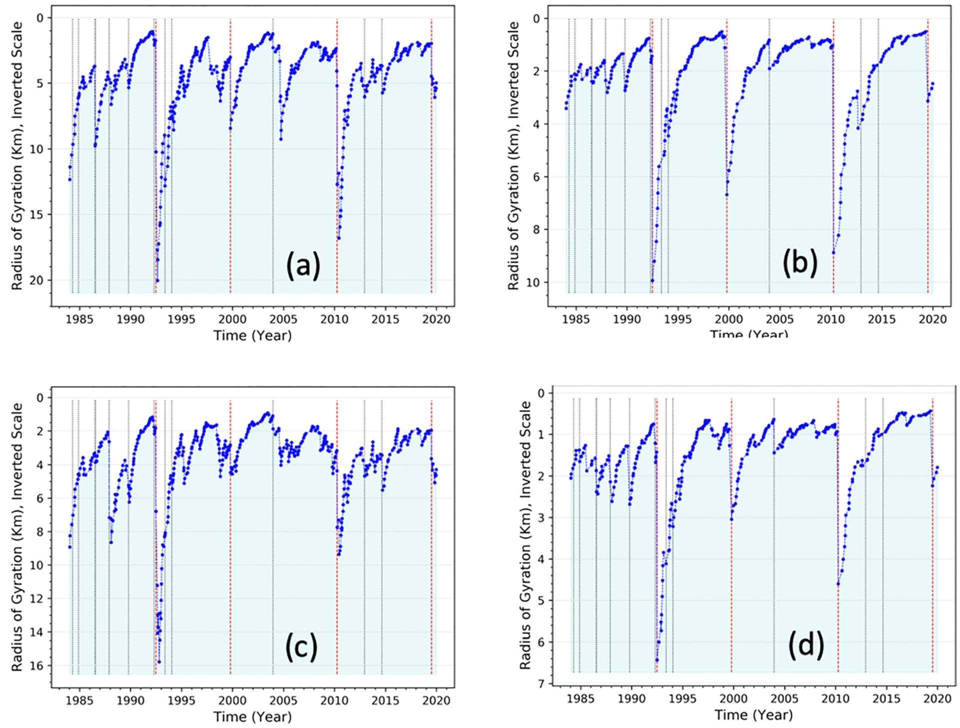

Figure 5. Examples of EMA time series similar to Figure 4 having different values for F_{EN} and F_{CL}. (a) $\text{Log}_{10}(F_{EN}) = -1.0$, $F_{CL} = 25$. (b) $\text{Log}_{10}(F_{EN}) = 0.2$, $F_{CL} = 25$. (c) $\text{Log}_{10}(F_{EN}) = -1.0$, $F_{CL} = 10$. (d) $\text{Log}_{10}(F_{EN}) = 0.2$, $F_{CL} = 10$.

for each day since 1 January 1984 to the present. Once we have these interpolated time series in hand, we compute the EMA mean value of R_G for each day, together with its standard deviation.

Figure 6 is the result of this process. Here we have used a Monte Carlo approach to optimize over the ensemble of filtered time series defined by the values F_{CL} = [5,10,15,20,25], and $\text{Log}_{10}(F_{EN})$ = [−1.0,

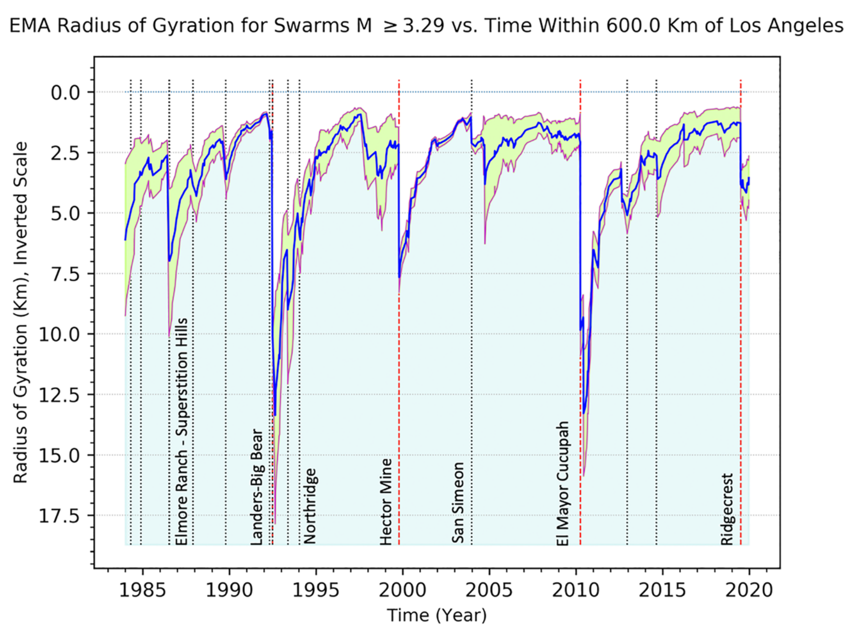

Figure 6. Ensemble time series for the exponential moving average (EMA) radius of gyration of bursts in the region using equal-weighted values for F_{EN} and F_{CL} as discussed in the text. A few of the prominent large earthquakes are indicated (Table 1). A value $N = 23$ was used to construct the EMAs that make up the components of the time series (see text).

23335084, 2020, 9, Downloaded from https://agupubs.onlinelibrary.wiley.com/doi/10.1029/2020EA001097 by Birla Institute of Technology & Science - Pilani, Wiley Online Library on [27/06/2024]. See the Terms and Conditions (https://onlinelibrary.wiley.com/terms-and-conditions) on Wiley Online Library for rules of use; OA articles are governed by the applicable Creative Commons License

10.1029/2020EA001097

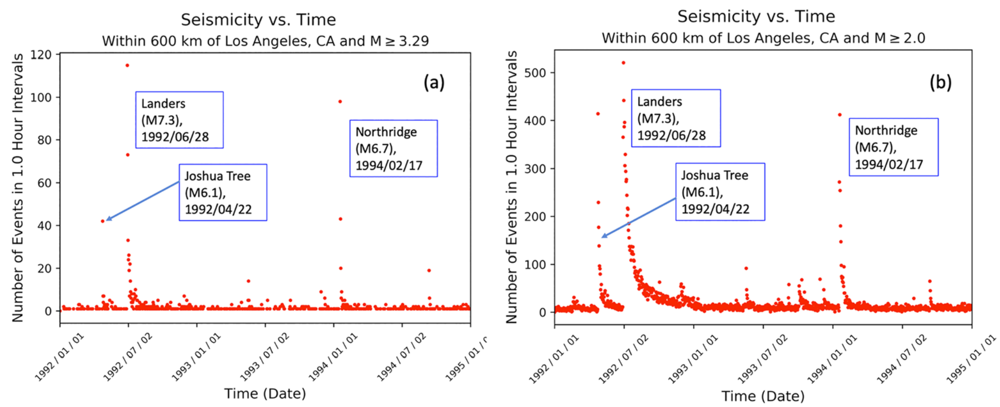

Figure 7. Number of small earthquakes in 1-hr time intervals during 1992–1995 within the 600-km region surrounding Los Angeles. (a) Minimum magnitude used was $M \geq 3.29$, the value used in previous plots here. (b) Minimum magnitude used was $M \geq 2$ for comparison. In both cases, the rate of decline in numbers to background rate is much faster than the rate of decline in horizontal radius of gyration shown in Figure 6.

$-0.9,-0.8,...,0.2]$. The values of the time series for radius of gyration for the four $M \geq 7$ earthquakes (Landers, Hector Mine, El Major Cucupah, and Ridgecrest) are 1.61 ± 0.11, 2.05 ± 0.7, 1.70 ± 0.77, and 1.18 ± 0.64 km. Mean and standard error of the mean are 1.65 ± 0.31 km for the radius of gyration just prior to the time of occurrence of the $M \geq 7$ earthquakes.

To a first approximation, our simple cost function yields an ensemble average consisting of equal weights of the constituent time series. These values are not unique, but in varying these filter parameters, we find no significant differences in the results.

In Figure 6, the solid blue curve represents the time-dependent mean of the R_G ensemble. The green band at the top records the time-dependent 1σ (1 standard deviation or 68% confidence interval) of the ensemble mean for each time. The similarities between Figures 3–6 are clear.

There is a recharge period where average R_G decreases prior to each magnitude $M \geq 7$, followed by a sudden discharge where R_G increases in average due to the large aftershock bursts following the mainshock. Between these large mainshocks, it can be seen that lesser-magnitude earthquakes result in lesser but similar effects. We discuss these results in the following section.

3.4. Physical Mechanism

An important question would be to understand the physics underlying radial localization. At the present time, we do not fully understand the mechanics of the process; rather, it must stand as an unexplained observation at this time.

However, we speculate as to the origins of the process. We do know that earthquake faults are organized in a hierarchy of groups with a fractal distribution of scales (Turcotte, 1997). Small faults are also known to be mechanically stiffer than large faults (e.g., Scholz, 2019), in that it takes a higher applied stress to produce the same slip.

Our speculation is therefore that as the regional tectonic stress increases, smaller faults and groups of faults are activated, leading to the observed radial localization. An alternative interpretation is that there is a natural clustering of background seismicity in Southern California that results in a R_G value of ~2 km, and this background value is perturbed whenever there is a large earthquake. This idea is discussed in more detail below.

4. Discussion and Conclusions

Our purpose in this research has been to connect the time of occurrence of the largest earthquakes in California since 1984 with a readily observable property of small earthquake seismicity in the region so as to improve upon earthquake nowcasting. We have therefore focused on bursts of small earthquake seismicity, which include both aftershocks of large earthquakes and small earthquake swarms. Improved machine

23335084, 2020, 9, Downloaded from https://agupubs.onlinelibrary.wiley.com/doi/10.1029/2020EA001097 by Birla Institute of Technology & Science - Pilani, Wiley Online Library on [27/06/2024]. See the Terms and Conditions (https://onlinelibrary.wiley.com/terms-and-conditions) on Wiley Online Library for rules of use; OA articles are governed by the applicable Creative Commons License

10.1029/2020EA001097

learning methods involving classification of the small earthquake seismicity, filtering, and optimization can probably systematically improve upon our results.

Other methods that may be applied could include decision tree analysis and deep learning (https://en.wikipedia.org/wiki/Machine_learning). Both of these depend on the construction of labeled feature vectors ($\boldsymbol{X}$,y). In our case, the vector $\boldsymbol{X}$ will be composed of seismicity measures, and the labels would include, for example, whether data in a particular feature vector are a precursor of a major earthquake within a specified time frame ($y = 1$) or not ($y = 0$).

We have discussed a process that we call radial localization of small earthquake bursts, which we define to be the gradual decrease of radius of gyration of these bursts prior to large earthquakes. We distinguish this from the idea of spatial localization that has been proposed previously as a precursor to large earthquakes (e.g., Kossobokov & Keilis-Borok, 1990), and which we discuss below.

The elastic rebound theory of earthquakes (Richter, 1958) proposes that tectonic stresses build up, recharge, or increase, in a region following a large earthquake until another large earthquake occurs, and stress discharges or decreases. At that point the stresses are suddenly reduced, and a new cycle of stress recharge and discharge begins. By presenting our results in the manner shown in Figures 3–6, the similarity with the elastic rebound theory can be seen.

The alternate hypothesis mentioned above might ascribe the decrease in radius of gyration as arising from only a simple manifestation of Omori's law, the decay of aftershocks following a mainshock. The aftershocks of this earthquake might then cluster densely and over a wide area, raising R_G for a period of time, following Omori's law (Omori, 1894). To investigate this possibility, we show the decay of aftershock numbers following the 1992 Landers earthquake in Figures 7a and 7b.

Figure 7a plots the number of $M \geq 3.29$ earthquakes between 1992 and 1995 in the study area, and Figure 7b plots the number of $M \geq 2$ earthquakes in the same region. $M \geq 3.29$ is the minimum magnitude used in Figure 6 and previous plots. As can be seen, the rate of decline of the aftershock numbers in either plot is much faster than the decrease in horizontal radius of gyration as shown in Figure 6; thus, the timescales are very different. We therefore conclude that simple decay of aftershocks is not sufficient to explain the phenomenon we observed here.

Our present results contribute to the development of seismic nowcasting methods that we have discussed earlier (Rundle et al., 2016, 2018; Rundle, Giguere, et al., 2019; Rundle, Luginbuhl, et al., 2019). In the previous methods, elastic rebound is introduced as a constraint, by counting small earthquakes since the last large earthquake. In contrast using this method, elastic rebound emerges naturally, in that it follows directly from time-dependent properties of the bursts. Another difference is that the seismic nowcasting method produces a cumulative distribution function, or equivalently a survivor distribution of future large earthquake activity. By contrast, the present method computes an observable property of the region with a clear physical meaning.

Of interest is the observation that the minimum radius of gyration (minimum R_G) prior to $M \geq 7$ mainshocks is typically 1 to 2 km. Achievement of each of these R_G values was followed within 1 to 3 years by an $M \geq 7$ earthquake, the only exception being the M6.5 22 December 2003 San Simeon earthquake. However, the time series recovered from that event and soon evolved toward the minimum R_G again. It should also be emphasized that *no $M \geq 7$ earthquakes have been observed at R_G values greater than the ensemble mean value of 2.5 km*. For that reason, $R_G \leq 2.5$ km can be considered to define a “low risk” threshold for $M \geq 7$ earthquakes.

Note also that our analysis uses only horizontal separation of earthquake epicenters in defining the radius of gyration, thus a 2-D measure. We have made this choice in California, where most earthquakes are shallow. However, in other parts of the world, such as subduction zones, it may be more appropriate to define 3-D radii of gyration for the clusters, a point we plan to investigate in the future.

The issue of spatial localization, mentioned above, has been a recurring topic in the literature for many years. Field, laboratory, statistical, and theoretical investigations have all examined processes associated with the onset of earthquakes and laboratory fracture. A very partial list of previous works includes the following.

23335084, 2020, 9, Downloaded from https://agupubs.onlinelibrary.wiley.com/doi/10.1029/2020EA001097 by Birla Institute of Technology & Science - Pilani, Wiley Online Library on [27/06/2024]. See the Terms and Conditions (https://onlinelibrary.wiley.com/terms-and-conditions) on Wiley Online Library for rules of use; OA articles are governed by the applicable Creative Commons License

10.1029/2020EA001097

- In the area of laboratory experiments, the emphasis has been on recording acoustic emissions in rock fracture experiments (Gao et al., 2019; Garcimartın et al., 1997; Lockner, 1993; Scholz, 1968; Wawersik & Fairhurst, 1970; Yong & Wang, 1980).
- Slip localization in laboratory friction experiments (Dieterich, 1986, 1992; Dieterich & Kilgore, 1995).
- In the area of field measurements, there have been many searches for foreshocks of large earthquakes (e.g., Kelleher et al., 1973; Kossobokov & Keilis-Borok, 1990; Richter, 1958; Scholz, 2019; Skordas et al., 2020; Vallianatos et al., 2012; Wyss et al., 1999, and many others referenced therein), defined as smaller earthquakes that immediately precede mainshocks in the source region.
- In the area of statistical properties of small earthquakes, other investigations have focused on understanding the statistics of links associated with clusters of small earthquakes (Main & Al-Kindy, 2002; Zaliapin & Ben-Zion, 2013, 2016a, 2016b; Zaliapin et al., 2008).
- In the area of theoretical investigations, there have been proposals of nonlinear material constitutive equations that demonstrate collapse of strain onto the eventual fracture rupture surface (Rudnicki & Rice, 1975; Shaw et al., 1992).

All of these studies have generally found results that have proven elusive when applied to field observations associated with earthquakes. As an example, it has been stated that only about 5% of all major earthquakes demonstrate foreshock activity (https://www.usgs.gov/faqs/what-probability-earthquake-a-foreshock-a-larger-earthquake?qt-news_science_products=0#qt-news_science_products). For that reason, spatial localization and premainshock elevated activity has generally not been found to be a property associated with major earthquakes, despite previous expectations.

At the current time, our study has not as yet seen reliable *spatial localization* of burst activity prior to mainshocks during the short times of days-weeks-months leading up to these major earthquakes. The search for these events is a work in progress at the present time, although there are some suggestions of potential signals. We plan to address this question in future work.

Other studies have shown that large earthquakes tend to occur in relatively small regions where small earthquake activity has been the greatest for a number of years (Holliday, Rundle, Tiampo, & Donnellan, 2006; Holliday, Rundle, Turcotte, et al., 2006; Holliday et al., 2007, 2008; Rundle et al., 2003; Tiampo, Rundle, Gross, et al., 2002; Tiampo, Rundle, McGinnis, Gross, & Klein, 2002; Tiampo, Rundle, McGinnis, & Klein, 2002). This is essentially a consequence of the universal applicability of the Gutenberg-Richter relation (Rundle et al., 2016, 2018). The RELM earthquake forecasting test suggests that this approach may be fruitful (Holliday et al., 2007; Lee et al., 2011).

We might therefore suggest a strategy to anticipate major earthquakes that combines methods such as those proposed by (e.g., Rundle et al., 2003) to estimate candidates for spatial locations of future events, combined with the ensemble time series methods discussed here. Or in other words, a time series such as that in Figure 4 might be combined with these likely location methods to determine times and candidate locations most at risk for future major earthquakes.

A question that remains is the applicability of the methods described here to other seismically active regions, which in turn depends on the completeness of the seismic catalog over a wide range of magnitudes. A major advantage of the Southern California region is that the catalog is complete to small magnitudes, a property that is not generally the case elsewhere. While we have not examined this question in detail, we have seen promise in preliminary applications of this method to Japan. Future work will be directed at answering this question.

Data Availability Statement

The data used in this paper were downloaded from the online earthquake catalogs (https://earthquake.usgs.gov/earthquakes/search/) maintained by the U.S. Geological Survey accessed between June through 20 December 2019.

Conflict of Interest

None of the authors have identified financial conflicts of interest.

23335084, 2020, 9, Downloaded from https://agupubs.onlinelibrary.wiley.com/doi/10.1029/2020EA001097 by Birla Institute of Technology & Science - Pilani, Wiley Online Library on [27/06/2024]. See the Terms and Conditions (https://onlinelibrary.wiley.com/terms-and-conditions) on Wiley Online Library for rules of use; OA articles are governed by the applicable Creative Commons License

Acknowledgments
The research of J. B. R. was supported in part by NASA Grant (NNX17AI32G) to UC Davis (nowcasting) and in part by DOE grant (DOE DE-SC0017324) to UC Davis (data analysis). Portions of the research by Andrea Donnellan were carried out at the Jet Propulsion Laboratory, California Institute of Technology, under a contract with the National Aeronautics and Space Administration. We thank colleagues including Donald Turcotte for helpful discussions, as well as helpful reviews from two anonymous referees.

References

Bahar, H. K., Tanami, S., Landen, S., Chapal, M., Szlak, L., Hutzler, A., et al. (2015). Bursty gene expression in the intact mammalian liver. *Molecular Cell*, *58*(1), 147–156. https://doi.org/10.1016/j.molcel.2015.01.027

Dieterich, J. H. (1986). A model for the nucleation of earthquake slip. In M. Ewing (Ed.), *Earthquake source mechanics*, *Geophysical Monograph 37* (Vol 6, pp. 37–47). Washington, DC: American Geophysical Union.

Dieterich, J. H. (1992). Earthquake nucleation on faults with rate- and state-dependent strength. *Tectonophysics*, *211*(1-4), 115–134. https://doi.org/10.1016/0040-1951(92)90055-B

Dieterich, J. H., & Kilgore, B. (1995). Implications of fault constitutive properties for earthquake prediction, presented at a colloquium entitled "Earthquake prediction: The scientific challenge," organized by Leon Knopoff (Chair), Keiiti Aki, Clarence R. Allen, James R. Rice, and Lynn R. Sykes, held February 10 and 11, at the National Academy of Sciences in Irvine, CA.

Gao, K., Guyer, R., Rougier, E., Ren, C. X., & Johnson, P. A. (2019). From stress chains to acoustic emissions. *Physical Review Letters*, *123*(4), 048003. https://doi.org/10.1103/PhysRevLett.123.048003

Garcimartın, A., Guarino, A., Bellon, L., & Ciliberto, S. (1997). Statistical properties of fracture precursors. *Physical Review Letters*, *79*(17), 3202–3205. https://doi.org/10.1103/PhysRevLett.79.3202

Hill, D. P. & Prejean, S. G., Dynamic triggering, in *Earthquake seismology*, vol. 4, G. Schubert, H. Kanamori, Eds. *Treatise on geophysics*, Schubert, G. (Editor-in Chief) (Elsevier, Amsterdam), pp. 257–291 (2007).

Holliday, J. R., Chen, C. C., Tiampo, K. F., Rundle, J. B., Turcotte, D. L., & Donnellan, A. (2007). A RELM earthquake forecast based on pattern informatics. *Seismological Research Letters*, *78*(1), 87–93. https://doi.org/10.1785/gssrl.78.1.87

Holliday, J. R., Rundle, J. B., Tiampo, K. F., & Donnellan, A. (2006). Systematic procedural and sensitivity analysis of pattern informatics method for forecasting large ($M > 5$) earthquake events in Southern California. *Pure and Applied Geophys*, *163*(11–12), 2433–2454. https://doi.org/10.1007/s00024-006-0131-1

Holliday, J. R., Rundle, J. B., Turcotte, D. L., Klein, W., & Tiampo, K. F. (2006). Space-time correlation and clustering of major earthquakes. *Physical Review Letters*, *97*(23), 238501. https://doi.org/10.1103/PhysRevLett.97.238501

Holliday, J. R., Turcotte, D. L., & Rundle, J. B. (2008). Self-similar branching of aftershock sequences. *Physica*, *A387*, 933–943.

Kelleher, J. A., Sykes, L. R., & Oliver, J. (1973). Possible criteria for predicting earthquake locations and their applications to major plate boundaries of the Pacific and Caribbean. *Journal of Geophysical Research*, *78*(14), 2547–2585. https://doi.org/10.1029/JB078i014p02547

Kossobokov, V. G., & Keilis-Borok, V. I. (1990). Localization of intermediate term earthquake prediction. *Journal of Geophysical Research*, *95*(B12), 19,763–19,772. https://doi.org/10.1029/JB095iB12p19763

Kucherov, L., & Ryvkin, M. (2014). Fracture toughness of open-cell Kelvin foam. *International Journal of Solids and Structures*, *51*(2), 440–448. https://doi.org/10.1016/j.ijsolstr.2013.10.015

Lee, Y. T., Turcotte, D. L., Holliday, J. R., Sachs, M. K., Rundle, J. B., Chen, C. C., & Tiampo, K. F. (2011). Results of the Regional Earthquake Likelihood Models (RELM) test of earthquake forecasts in California. *Proceedings of the National Academy of Sciences of the United States of America*, *108*(40), 16,533–16,538. https://doi.org/10.1073/pnas.1113481108

Lockner, D. (1993). The role of acoustic emission in the study of rock fracture. *International Journal of Rock Mechanics and Mining Sciences & Geomechanics Abstracts*, *30*(7), 883–899. https://doi.org/10.1016/0148-9062(93)90041-B

Main, I. G., & Al-Kindy, F. H. (2002). Entropy, energy, and proximity to criticality in global earthquake populations. *Geophysical Research Letters*, *29*(7). https://doi.org/10.1029/2001GL014078

Mantegna, R. N., & Stanley, H. E. (2004). *An introduction to Econophysics, correlations and complexity in finance*. Cambridge, UK: Cambridge University Press.

Omori, F. (1894). *On the aftershocks of earthquakes: Journal of the College of Science*. Tokyo, Japan: Imperial University of Tokyo.

Paczuski, M., Maslov, S., & Per Bak, P. (1996). Avalanche dynamics in evolution, growth, and depinning models. *Physical Review E*, *53*(1), 414–443. https://doi.org/10.1103/PhysRevE.53.414

Pasari, S. (2019). Nowcasting earthquakes in the bay of Bengal region. *Pure and Applied Geophysics*, *176*(4), 1417–1432. https://doi.org/10.1007/s00024-018-2037-0

Peresan, A., & Gentili, S. (2018). Seismic clusters analysis in Northeastern Italy by the nearest-neighbor approach. *Physics of the Earth and Planetary Interiors*, *274*, 87–104. https://doi.org/10.1016/j.pepi.2017.11.007

Reasenberg, P. (1985). Second-order moment of central California seismicity, 1969–1982. *Journal of Geophysical Research*, *90*(B7), 5479–5495. https://doi.org/10.1029/JB090iB07p05479

Richter, C. F. (1958). *Elementary seismology*. New York: WH Freeman.

Rudnicki, J. W., & Rice, J. R. (1975). Conditions for the localization of deformation in pressure-sensitive dilatant materials. *Journal of the Mechanics and Physics of Solids*, *23*(6), 371–394. https://doi.org/10.1016/0022-5096(75)90001-0

Rundle, J. B., Giguere, A., Turcotte, D. L., Crutchfield, J. P., & Donnellan, A. (2019). Global seismic nowcasting with Shannon information entropy. *Earth and Space Science*, *6*, 456–472.

Rundle, J. B., Luginbuhl, M., Giguere, A., & Turcotte, D. L. (2018). Natural time, nowcasting and the physics of earthquakes: Estimation of risk to global megacities. *Pure and Applied Geophysics*, *175*(2), 647–660. https://doi.org/10.1007/s00024-017-1720-x

Rundle, J. B., Luginbuhl, M., Khapikova, P., Turcotte, D. L., Donnellan, A., & McKim, G. (2019). Nowcasting great global earthquake and tsunami sources. *Pure and Applied Geophysics*, *177*(1), 359–368. https://doi.org/10.1007/s00024-018-2039-y

Rundle, J. B., Tiampo, K. F., Klein, W., & Martins, J. S. S. (2002). Self-organization in leaky threshold systems: The influence of near mean field dynamics and its implications for earthquakes, neurobiology and forecasting. *Proceedings of the National Academy of Sciences USA*, *99*(Supplement 1), 2514–2521.

Rundle, J. B., Turcotte, D. L., Donnellan, A., Grant Ludwig, L., Luginbuhl, M., & Gong, G. (2016). Nowcasting earthquakes. *Earth and Space Science*, *3*(11), 480–486. https://doi.org/10.1002/2016EA000185

Rundle, J. B., Turcotte, D. L., Sammis, C., Klein, W., & Shcherbakov, R. (2003). Statistical physics approach to understanding the multiscale dynamics of earthquake fault systems (invited). *Reviews of Geophysics Space Phys*, *41*(4). https://doi.org/10.1029/2003RG000135

Sayers, C. M., & Calvez, J. L. (2010). Characterization of microseismic data in gas shales using the radius of gyration tensor. In *SEG Technical Program Expanded Abstracts 2010* (pp. 2080-2084). Society of Exploration Geophysicists.

Scholz, C. H. (1968). Microfracturing and the inelastic deformation of rock in compression. *Journal of Geophysical Research*, *73*(4), 1417–1432. https://doi.org/10.1029/JB073i004p01417

Scholz, C. H. (2019). *The mechanics of earthquakes and faulting*. Cambridge, UK: Cambridge University Press.

Shaw, B. E., Carlson, J. M., & Langer, J. S. (1992). Patterns of seismic activity preceding large earthquakes. *Journal of Geophysical Research*, *97*(B1), 479–488. https://doi.org/10.1029/91JB01796

23335084, 2020, 9, Downloaded from https://agupubs.onlinelibrary.wiley.com/doi/10.1029/2020EA001097 by Birla Institute of Technology & Science - Pilani, Wiley Online Library on [27/06/2024]. See the Terms and Conditions (https://onlinelibrary.wiley.com/terms-and-conditions) on Wiley Online Library for rules of use; OA articles are governed by the applicable Creative Commons License

10.1029/2020EA001097

Skordas, E. S., Christopoulos, S.-R. G., & Sarlis, N. V. (2020) Published online at). Detrended fluctuation analysis of seismicity and order parameter fluctuations before the *M*7.1 Ridgecrest earthquake. *Natural Hazards*, 1–15. https://doi.org/10.1007/s11069-019-03834-7

Tiampo, K. F., Rundle, J. B., Gross, S. J., McGinnis, S., Gross, S., & Klein, W. (2002). Eigenpatterns in Southern California seismicity. *Journal of Geophysical Research*, *107*(B12), 2354. https://doi.org/10.1029/2001JB000562

Tiampo, K. F., Rundle, J. B., McGinnis, S., Gross, S., & Klein, W. (2002). Mean field threshold systems and phase dynamics: An application to earthquake fault systems. *Europhysics Letters*, *60*(3), 481–488. https://doi.org/10.1209/epl/i2002-00289-y

Tiampo, K. F., Rundle, J. B., McGinnis, S., & Klein, W. (2002). Pattern dynamics and forecast methods in seismically active regions. *Pure and Applied Geophysics*, *159*(10), 2429–2467. https://doi.org/10.1007/s00024-002-8742-7

Turcotte, D. L. (1997). *Fractals and chaos in geology and geophysics*. Cambridge: Cambridge University Press. https://doi.org/10.1017/CBO9781139174695

Vallianatos, F., Michas, G., Papadakis, G., & Sammonds, P. (2012). A nonextensive statistical physics view to the spatiotemporal properties of the June 1995, Aegean earthquake (*M*6. 2) aftershock sequence (West Corinth rift, Greece). *Acta Geophysica*, *60*(3), 758–768. https://doi.org/10.2478/s11600-012-0011-2

Wawersik, W. R., & Fairhurst, C. (1970). A study of brittle rock fracture in laboratory compression experiments. *International Journal of Rock Mechanics and Mining Sciences*, *7*(5), 561–575. https://doi.org/10.1016/0148-9062(70)90007-0

Wyss, M., Shimazaki, K., & Ito, A. (1999). *Seismicity patterns their statistical significance and physical meaning, Pure and Applied Geophysics*. Basel, Switzerland: Topical Volume, Birkhauser. https://doi.org/10.1007/978-3-0348-8677-2

Yong, C., & Wang, C.-Y. (1980). Thermally induced acoustic emission in Westerly granite. *Geophysical Research Letters*, 1089–1092.

Zaliapin, I., & Ben-Zion, Y. (2013). Earthquake clusters in Southern California I: Identification and stability. *Journal of Geophysical Research: Solid Earth*, *118*, 2865–2877.

Zaliapin, I., & Ben-Zion, Y. (2016a). Discriminating characteristics of tectonic and human-induced seismicity. *Bulletin of the Seismological Society of America*, *106*(3), 846–859. https://doi.org/10.1785/0120150211

Zaliapin, I., & Ben-Zion, Y. (2016b). A global classification and characterization of earthquake clusters. *Geophysical Journal International*, *207*(1), 608–634. https://doi.org/10.1093/gji/ggw300

Zaliapin, I., Gabrielov, A., Keilis-Borok, V., & Wong, H. (2008). Clustering analysis of seismicity and aftershock identification. *Physical Review Letters*, *101*(1), 018501. https://doi.org/10.1103/PhysRevLett.101.018501

23335084, 2020, 9, Downloaded from https://agupubs.onlinelibrary.wiley.com/doi/10.1029/2020EA001097 by Birla Instiute of Technology & Science - Pilani, Wiley Online Library on [27/06/2024]. See the Terms and Conditions (https://onlinelibrary.wiley.com/terms-and-conditions) on Wiley Online Library for rules of use; OA articles are governed by the applicable Creative Commons License